4   **Atomistic mechanism of cadmium incorporation into hydroxyapatite**

5

6   Huan Liu[1], Xiancai Lu[1],*, Xiangjie Cui[1], Lijuan Zhang[2], Ting-Shan Chan[3]

7

8   [1]Key Laboratory of Surficial Geochemistry, Ministry of Education, School of Earth Sciences and

9   Engineering, Nanjing University, Nanjing, Jiangsu 210023, China

10 [2]Shanghai Synchrotron Radiation Facility, Shanghai Advanced Research Institute, Chinese

11 Academy of Sciences, Shanghai 201204, China

12 [3]National Synchrotron Radiation Research Center, Hsinchu 30076, Taiwan

13

14 * Corresponding author: xcljun@nju.edu.cn (Xiancai Lu). Tel: +86-25-89681065.

15

16

17

18

19

20

21 Submitted to *American Mineralogist*

22 April 2020

23

24

Abstract

25

26   Hydroxyapatite (HAp) has been widely used to remove cadmium (Cd) in contaminated

27   water and soils via Cd-Ca substitution. The Cd incorporation into HAp affects its structure;

28   however, the detailed mechanism remains unclear. In this study, a series of Cd-substituted

29   hydroxyapatites were synthesized and characterized with various techniques. Cd incorporation

30   causes a decrease in a- and c-lattice parameters due to the radius of Cd^{2+} being slightly smaller

31   than that of Ca^{2+}. As the Cd content increases, the particle sizes of the synthesized samples

32   decrease and their specific surface areas increase. Raman bands shift linearly and the $v_1(PO_4)$

33   peak at 961 cm^{-1} become broadened with increasing Cd content. Change in X-ray absorption

34   near edge structure (XANES) spectra of the P K-edge indicates distortion of phosphate with Cd

35   incorporation. Total electron yield (TEY) spectra of the Ca $L_{2,3}$-edge show a decrease in the

36   octahedral symmetry, suggesting preferential occupancy of Cd over the Ca2 site. Extended X-ray

37   absorption fine structure (EXAFS) analysis of the Ca K-edge reveals no obvious change in the

38   local environment of Ca induced by Cd incorporation. However, EXAFS analysis of the Cd K-

39   edge indicates that the substituted Cd occupies one Ca2 site in hexagonal Ca2 positions at low

40   Cd contents (<10 mol% of Cd/(Cd+Ca)), while both Ca1 and Ca2 sites are occupied at higher Cd

41   contents. This study provides atomistic insight into the mechanism for Cd incorporation in HAp,

42   which will help develop an approach for effective Cd removal using HAp for environmental

43   remediation.

44

45   **Keywords:** Hydroxyapatite (HAp), Cadmium, EXAFS, Raman, Incorporation mechanism

46   **INTRODUCTION**

47   Hydroxyapatite (HAp, $Ca_{10}(PO_4)_6(OH)_2$) is one of the most common apatite-group minerals

48   in nature, particularly important in biological systems, such as bones, teeth, and fossils (Wilson

49   et al., 1999). HAp is also crucial in biological mineralization processes and controls the

50   geochemical cycle of P in soils and sediments (Goldhammer et al., 2010; Zhang et al., 2010).

51   Natural apatites commonly contain foreign cations and/or anions substituted in mineral structures

52   because of their remarkable tolerance to structural distortion, making apatite-group minerals

53   extremely diverse in chemical composition. Many common cations and anions have been shown

54   to be incorporated into HAp, such as Mg^{2+}, Sr^{2+}, Mn^{2+}, Cd^{2+}, CO_3^{2-}, SiO_4^{4-}, Cl^-, and F^- (Hughes

55   and Rakovan, 2015; Kim et al., 2017; Pan and Fleet, 2002). Among these substitutions, a large

56   number of divalent cations have been reported to occupy Ca sites and alter the structure and

57   properties of HAp, such as lattice parameters (Hughes and Rakovan, 2015; Lala et al., 2015; Pan

58   and Fleet, 2002). Several cations can even form a complete solid-solution of HAp (Pan and Fleet,

59   2002). Such a property provides a potential in environmental applications, because the

60   incorporation of toxic metals into mineral structure could make metals remain stable in the solid

61   phase, thus achieving long-term remediation (Bailey et al., 2005).

62   Cadmium (Cd) is highly toxic and a carcinogen harmful to human health. It can be taken in

63   human body through drinking water and nutrition, and retain in bones by replacing Ca in

64   hydroxyapatite, which commonly causes serious "Itai-itai" disease (Kobayashi, 1978;

65   McLaughlin and Singh, 1999). In nature, Cd usually diffuses into soils and water via

66   atmospheric deposition, phosphate fertilizers, and sewage sludge application, causing serious Cd

67   contamination (McLaughlin and Singh, 1999). Ca phosphate, especially HAp, is commonly used

68   to remove heavy metals from contaminated water and soils (Bailey et al., 2005; da Rocha et al.,

69 2002; Peld et al., 2004; Srinivasan et al., 2006; Wang et al., 2019; Xu et al., 1994). Cd can co-

70 precipitate with Ca phosphate via isomorphic substitution, which is normally more effective than

71 surface adsorption (Bailey et al., 2005; Valsami-Jones et al., 1998). Furthermore, phosphate has

72 been widely used as a fertilizer for plants in soils, leading to precipitation of Cd-bearing Ca

73 phosphate in soils (McLaughlin and Singh, 1999). Thus, mixing phosphate with metal-

74 contaminated soils to form metal-Ca phosphate has been well established as an in-situ technique

75 for environmental remediation (Lee et al., 2018; Skwarek and Janusz, 2016). In addition, in

76 many phosphate ores, Cd was commonly found to be incorporated in apatite structures (Sery et

77 al., 1996). Understanding the mechanism of Cd incorporation into HAp could help us better

78 understand Cd geochemical behaviors and the application of HAp for Cd remediation in Cd-

79 contaminated environment.

80   HAp has a hexagonal structure with space group $P6_3/m$ (Kay et al., 1964). HAp has two

81 nonequivalent Ca sites: Ca1 is nine O coordinated (six O-Ca in less than 2.55 Å and three more

82 distant), while Ca2 is surrounded by seven oxygen atoms with six from five phosphates and one

83 hydroxyl oxygen atom (Figure S1) (Laurencin et al., 2011; Sery et al., 1996). The molar ratio of

84 Ca1 to Ca2 is 2:3, thus the chemical formula of HAp can be written as $Ca1_4Ca2_6(PO_4)_6(OH)_2$

85 (Zilm et al., 2016; Zougrou et al., 2016). The preferred Ca site for cation substitution and the

86 incorporated mechanism remain unclear. Cd^{2+} can completely occupy all Ca sites in HAp and

87 form complete solid-solutions from $Ca_{10}Cd_0(PO_4)_6(OH)_2$ to $Ca_0Cd_{10}(PO_4)_6(OH)_2$ due to their

88 similar radii (Bigi et al., 1986; Lanfranco et al., 2003; Pan and Fleet, 2002; Zhu et al., 2016).

89 Thus, Cd atoms could occupy both Ca1 and Ca2 sites in HAp (Hata et al., 1978), and the

90 substituted sites will change from one Ca site to both sites as the Cd content increases (Zhu et al.,

91 2016). However, the concentration of Cd in soils or phosphate ores is commonly insufficient to

92   form pure Cd end members of HAp and only Cd-bearing Ca-HAp can be found (Bailey et al.,

93   2005; Sery et al., 1996). Thus, understanding the site preference of Cd incorporation into HAp is

94   helpful to understand the occurrence of Cd in phosphate-treated Cd-contaminated soils.

95   The occurrence of Cd in HAp has been investigated by numerous techniques, and the

96   distribution of Cd at Ca1 and Ca2 sites is still under debate. An extended X-ray absorption fine

97   structure (EXAFS) analysis indicates that Cd in apatite from phosphate ores occupies both Ca

98   sites with a slight preference for the Ca2 site (Sery et al., 1996). However, other studies based on

99   X-ray diffraction (XRD) and EXAFS analysis suggest that Cd occurs at both Ca sites without

100   any site preference even at low Cd concentrations, and disclose a linear correlation between

101   lattice parameters and Cd contents (Bailey et al., 2005; Lanfranco et al., 2003). It is worth noting

102   that density functional theory calculations have shown that the Ca2 site is favored due to its more

103   covalent properties (Tamm and Peld, 2006; Terra et al., 2010). Compared to other incorporated

104   ions, Cd has a similar radius to Ca, resulting in small changes in lattice parameters (*a* and *c* from

105   9.42 Å and 6.86 Å to 9.32 Å and 6.65 Å, respectively for Ca and Cd end members of HAp)

106   (Lanfranco et al., 2003). Additionally, most of EXAFS analyses have only been conducted on Cd

107   without considering the local environment of Ca in HAp, which is also related to the occupied

108   site preference. In this study, both Ca and Cd K-edge EXAFS analyses, total electron yield (TEY)

109   spectra of the Ca $L_{2,3}$-edge, and X-ray absorption near edge structure (XANES) spectra of the P

110   K-edge of synthesized Cd-substituted HAps with various molar ratios of Cd/(Cd+Ca) up to 0.2

111   were conducted to determine the effects of Cd incorporation on the local atomic environment of

112   Ca and P in HAp, as well as to reveal the mechanism of Cd incorporation.

113   **MATERIALS AND METHODS**

114   **Synthesis of HAp and Cd-substituted HAp samples**

115   HAp and Cd-substituted HAp (Cd-HAp) samples were synthesized according to the

116   reported method (Matsunaga et al., 2010), with dropwise addition of 0.1 M $(NH_4)_2HPO_4$ solution

117   into a mixed solution of 0.1 M $Ca(NO_3)_2 \cdot 4H_2O$ and 0.1 M $Cd(NO_3)_2$. The Cd/(Cd+Ca) molar

118   ratio of the mixed solution varied from 0.01 to 0.20, while the (Ca+Cd)/P ratio was maintained at

119   the stoichiometric ratio of 1.67. The pH of the reaction system was kept at 10 by continuously

120   adding ammonia solution. Obtained precipitates were aged for 48 h, then washed with distilled

121   water, centrifuged and dried at 60 °C for 24 h. According to initial Cd/(Cd+Ca) ratios of mixed

122   solutions, the synthesized samples were named as HAp, HAp-1Cd, HAp-5Cd, HAp-10Cd, and

123   HAp-20Cd (Table 1).

124   **Characterization techniques**

125   The precipitates were characterized using synchrotron X-ray diffraction (XRD) at an

126   incident energy of 18 keV with a wavelength of 0.6883 Å at beamline 14B of Shanghai

127   Synchrotron Radiation Facility (SSRF). XRD patterns were recorded in the 2θ range of 3-45°

128   using a line-detector model (Yang et al., 2015). Lattice parameters were refined with the GSAS

129   software package (Larson and Von Dreele, 2000) with the EXPGUI interface (Toby, 2001).

130   Initial unit-cell parameters for HAp were taken from Hughes et al. (1989).

131   The Ca, Cd, and P contents of the synthesized HAp samples were determined as follows: 10

132   mg of each Cd-HAp sample was digested in 10 mL of 2 M HNO_3 solution, and then Ca, Cd, and

133   P concentrations in the solution were measured by inductively coupled plasma optical emission

134   spectrometry (ICP-AES, Thermo Fisher Scientific 6300). The morphology of pure HAp and Cd-

135   HAp samples (HAp-10Cd) was characterized with a high-resolution transmission electron

136   microscope (HR-TEM, FEI TF20) operated at 200 kV acceleration voltage. Specific surface

137   areas (SSA) were calculated using the multipoint BET method based on nitrogen adsorption

138   isotherms with a p/p_0 range of 0.05−0.20 at 77 K, which were measured on a Micrometrics

139   ASAP 2020 apparatus after degassing at 80°C for at least 10 h. Raman spectra from 100 to 1400

140   cm^{-1} with a resolution of 0.5 cm^{-1} were collected at room temperature under a 50WL×objective

141   of a JY/Horiba LabRAM HR Raman system with a 532.11 nm laser excitation and an 1800-

142   groove/mm grating. Each spectrum was collected with five accumulations to improve the signal-

143   to-noise ratio.

144   TEY spectra of the Ca $L_{2,3}$-edge were collected in the total electron yield mode at beamline

145   08U1A of SSRF. Sample powders were dispersed on an aluminum foil with a plastic support.

146   The Ca $L_{2,3}$-edge spectra were acquired at an energy step of 0.1 eV with three averages per

147   spectrum (Zhang et al., 2015). XANES spectra of the P K-edge and EXAFS spectra of the Ca K-

148   edge of the synthesized samples were collected at beamline 16A1 at National Synchrotron

149   Radiation Research Center (NSRRC, Taiwan), with an electronic storage ring of 1.5 GeV and an

150   operating current of 360 mA. EXAFS data for the Cd K-edge in Cd-HAp samples were collected

151   at beamline 01C1 of NSRRC. EXAFS data were processed using the Athena and Artemis from

152   the IFEFFIT software package (Ravel and Newville, 2005). Back-scattering phase and amplitude

153   functions were calculated with FEFF 7.02 (Ankoudinov, 1996) from the crystal structure of HAp

154   (Hughes et al., 1989) for Ca spectra and partial Cd-for-Ca substitution for Cd spectra. Multiple

155   scattering effects were neglected for simplification, which has already been employed in the

156   study of Ca and Cd K-edge EXAFS spectra (Bailey et al., 2005; Harries and Hukins, 1986;

157   Lanfranco et al., 2003; Laurencin et al., 2011).

158   **RESULTS**

159   **Characterization of the mineral phases**

160   The Ca, Cd, and P contents in the synthesized samples (Table 1) indicate that (Cd+Ca)/P

161   molar ratios in all HAp samples are almost equal to the stoichiometric ratio of 1.67 and their

162   Cd/(Ca+Cd) molar ratios are similar to those of solutions, except for HAp-20Cd, in which the Cd

163   content is only 16.18 mol%. XRD patterns (Figure 1a) of all pure HAp and Cd-HAp samples

164   exhibit diffraction peaks of HAp, and no other phases are present. Differences in the peak

165   position, intensity and full width at half maximum (FWHM) of (002) are shown in Figure 1b

166   with an enlarged XRD pattern in the range of $11° \leq 2\theta \leq 16°$, which clearly shows the shift of

167   peak (002) to smaller d-spacing values and broader FWHM values with increasing Cd content

168   (Figure S2). The shift is not obvious in HAps with low Cd contents (HAp-1Cd and HAp-5Cd)

169   because of the high similarity between the radii of Cd^{2+} (0.095 nm) and Ca^{2+} (0.100 nm)

170   (Shannon, 1976). Lattice parameters a and c decrease slightly from 9.426 Å and 6.868 Å to

171   9.394 and 6.824 Å, respectively (Table 1), which are linearly correlated with Cd content (Figure

172   S3), indicating homogenous substitution (Lanfranco et al., 2003; Srinivasan et al., 2006; Terra et

173   al., 2010). The decrease in the intensity of peak (002) and the broadening in the peak width with

174   increasing Cd content indicate a decline in the degree of crystallization.

175

176   **Table 1.** Chemical compositions and refined lattice parameters

Samples	Initial Cd/(Cd+Ca) (mol%) in solution	Cd/(Cd+Ca) (mol%) in solids	(Cd+Ca)/P in solids	SSA (m²/g)	a (Å)	c (Å)	V (Å³)
HA	0	0.00	1.66	86.1	9.426(2)	6.868(2)	528.44(20)
HA-1Cd	1	1.00	1.68	98.0	9.424(2)	6.864(1)	527.96(18)
HA-5Cd	5	4.79	1.68	100.9	9.412(2)	6.852(1)	525.72(18)
HA-10Cd	10	9.14	1.69	113.8	9.402(1)	6.837(1)	523.36(15)
HA-20Cd	20	16.18	1.66	104.6	9.394(1)	6.824(1)	521.51(11)

177
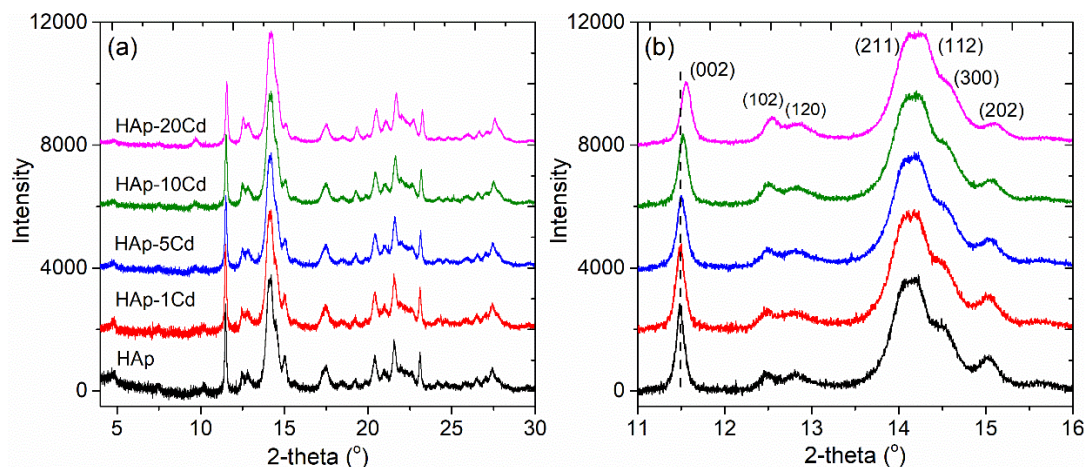
Figure 1. Synchrotron XRD patterns of pure HAp and Cd-HAp samples.

TEM images (Figure 2) show that all the synthesized HAp samples have spindle shapes, consistent with reported HAp crystals (Lowry et al., 2017). With an increase of Cd content in HAp, the particle sizes decrease from 50-60 nm (HAp) to <30 nm (HAp-10Cd), which explains the increase in SSA from 86.1 m^2/g (HAp) to 113.8 m^2/g (HAp-10Cd) (Table 1). The interplanar (002) spacing in HR-TEM images also decreases from 3.458 Å to 3.446 Å (Figure 2b, e), which is consistent with the (002) XRD peak's shifting to higher 2θ values (Figure S2). The selected area electron diffraction (SAED) pattern in Figure 2c, f shows that the (221) and (222) planes have strong diffraction intensities.
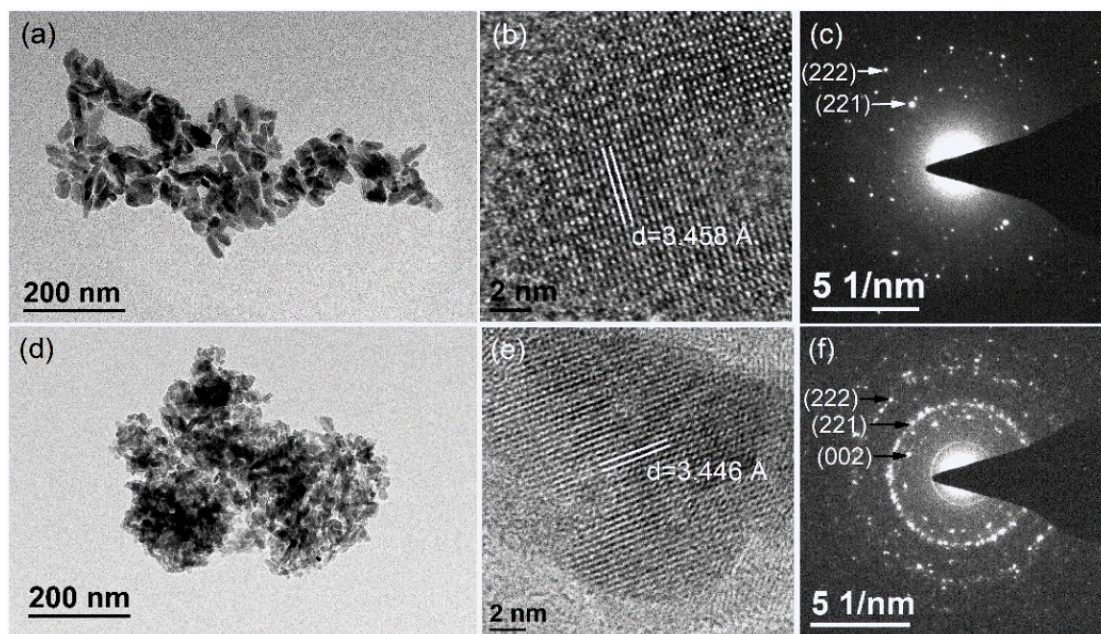
189

190   Figure 2. TEM images of pure HAp (a, b, and c) and HAp-10Cd (d, e, and f). (f) displays bright

191   rings from the SAED area (200 nm) that contains many crystals due to their small sizes.

192

193   **Raman spectra and P K-edge XANES spectra of synthesized HAps**

194   Local distortions of phosphate in the HAp structure induced by Cd incorporation are

195   investigated by Raman spectroscopy and XANES analysis. Normalized Raman spectra of pure

196   HAp and Cd-HAp samples (Figure 3a) and peak positions are consistent with typical bands of

197   the HAp phase, and model assignments are compiled in Table S1 (Antonakos et al., 2017;

198   Guerra-López et al., 2015). For all samples, the strong peak at 961 cm^{-1} has been assigned to the

199   symmetric v_1 stretching vibration of PO_4 groups, and peaks of three $v_3(PO_4)$, three $v_4(PO_4)$, and

200   two $v_2(PO_4)$ vibrations are also observed. The peak position of $v_1(PO_4)$ shifts slightly down to

201   lower wavenumbers (Figure 3b), and the FWHM values increase from 6.6 cm^{-1} to 12.9 cm^{-1} with

202   increasing Cd content (Table S1), showing linear correlations with substituted Cd (Figure S4). In

203   particular, as the Cd content increases, three peaks at ~579 cm^{-1}, 591 cm^{-1}, and 607 cm^{-1} assigned

204   to $v_4(PO_4)$ vibrations show a redshift, and the intensity ratio of two peaks at 579 and 591 cm^{-1}

205   increases. All of these changes indicate an increase in progressive distortion of tetrahedral

206   phosphate ions with Cd incorporation (Antonakos et al., 2007; Petit et al., 2017).

207
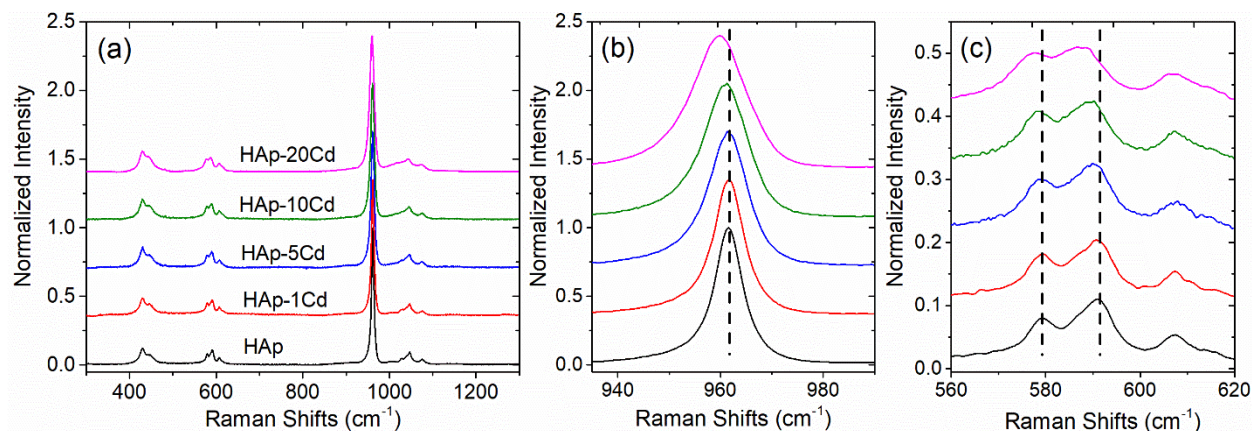
208

209   Figure 3. Raman spectra of pure HAp and Cd-HAp samples (a) and the magnified Raman spectra

210   in wavenumbers of 940-990 cm^{-1} (b) and 560-620 cm^{-1} (c). The highest intensity of all spectra

211   are normalized to be 1.0 for better comparison.

212

213   The P K-edge XANES spectra of pure HAp and Cd-HAp samples present the features of

214   four peaks, consistent with reported HAp phase (Figure S5) (Liu et al., 2017). For all Cd-HAp

215   samples, an edge jump (peak 1), a shoulder (peak 2) and two post-edge peaks (3 and 4) are at the

216   same energy positions, exhibiting same Ca-bound P environment (Prietzel et al., 2013). However,

217   the intensity of the shoulder related to peak 1 decreases slightly and progressively depicts an

218   increased structural disorder of HAp with increasing Cd content, which is thought to be induced

219   by the PO_4 groups bound with substituted Cd (Prietzel et al., 2013).

220   **Ca $L_{2,3}$-edge TEY spectra of synthesized HAps**

221   The energy positions of the main L_3 (a_2 at ~349.4 eV) and L_2 peaks (b_2 at ~352.7 eV), as

222   well as pre-edge peaks (hereafter called a_1 and b_1) in the Ca $L_{2,3}$-edge TEY spectra of all HAp

223   samples (Figure 4) are quite similar. Commonly, the split energy of a_1 and a_2 peaks is

224   proportional to the crystallinity of HAps (Beniash et al., 2009; Politi et al., 2008; Zougrou et al.,

225   2016). The split energy of pure HAp and Cd-HAps are similar to each other (Figure S6, Tables

226   S2), indicating little change in the crystallinity due to Cd incorporation, which is also shown in

227   XRD results. For pre-edge peaks, a_1 has been reported to represent the octahedral (O_h) symmetry

228   of Ca^{2+} caused by the 2p-3d spin-orbit coupling, mainly contributed from Ca2 sites (Cosmidis et

229   al., 2015; Naftel et al., 2001). The decrease in relative intensities (a_1/L_3 in Table S2) with Cd

230   content indicates that the O_h symmetry from the Ca2 site decreases with Cd incorporation,

231   suggesting that Cd has preferentially entered this site. This interpretation relies on the

232   assumption that the coordination environment (coordination numbers and bond distance) of Ca in

233   each site remains the same upon Cd incorporation (Laurencin et al., 2011). Given that the local

234   environment of Ca mainly depends on the Ca···O coordination, the average bond distance and

235   coordination number of Ca···O in the first sphere should be similar for all HAp samples. To

236   confirm this interpretation, EXAFS spectra of the Ca K-edge are analyzed to reveal the local

237   environment of Ca.
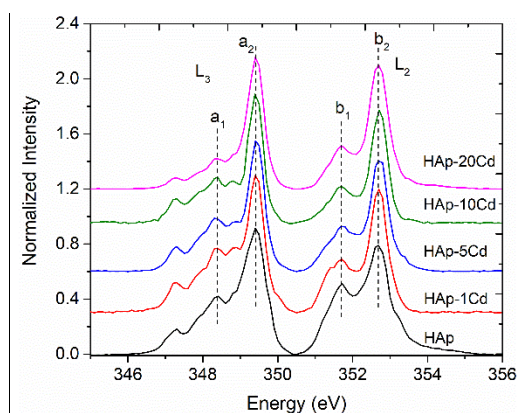
238

239   Figure 4. TEY spectra of the Ca $L_{2,3}$-edge in pure HAp and Cd-HAp samples.

240

241   **EXAFS spectra of the Ca K-edge in HAps**

242   The Ca K-edge XANES spectra of Cd-HAp samples are nearly identical to that of pure

243   HAp, except for a decrease in the shoulder peak intensity (Figure S7a). The XANES spectrum of

244   HAp-20Cd with the highest Cd content is nearly identical to that of pure HAp (Figure S7b),

245   especially in the pre-edge region, which is sensitive to the local distortion around Ca ions. The

246   pre-edge region at 4037 eV due to the 1s→3d electron transition is similar regardless of Cd

247   content, suggesting that the local environment of Ca atoms are similar in Cd-HAp samples

248   (Laurencin et al., 2011; Neuville et al., 2004).

249   EXAFS spectra of the Ca K-edge and structural fitting of HAp samples are shown in Figure

250   5 and listed in Table S3. The $k^3\chi(k)$ spectra and the Fourier transforms (FT) of HAp and Cd-

251   HAps are very similar, consistent with reported HAp spectra (Harries and Hukins, 1986; Harries

252   et al., 1988; Laurencin et al., 2011). Their Fourier transforms show three peaks with similar

253   intensity of the first peak at ~1.9 Å (indicated by P1 and not corrected for phase shifts) (Figure

254   5b), and the fitted bond distances and Debye-Waller factors (σ^2) are quite similar, suggesting that

255   the local geometry of the nearest Ca···O shell is not significantly modified by Cd incorporation.

256   For distant shells (>3 Å) contributed from the back-scattering of surrounding P, Ca, and more

257   distant O (Harries and Hukins, 1986; Laurencin et al., 2011), neither the spectra nor fitting

258   results show any noteworthy change due to Cd incorporation. For HAp-20Cd, the third peak (P3)

259   intensity is slightly stronger than that in HAp (Figure 5b). Given that this part of the spectrum

260   arises from Ca atoms, the increase in the P3 intensity could result from the presence of Cd atoms,

261   which are heavier and thus have stronger back-scattering than Ca. However, it is difficult to

262   evaluate any change in the long-range ordering around Ca due to slight difference among fitting

263   parameters (Table S3). The low Cd content and similar ion radii of Cd^{2+} and Ca^{2+} hardly modify

264   the local environment of Ca.

265
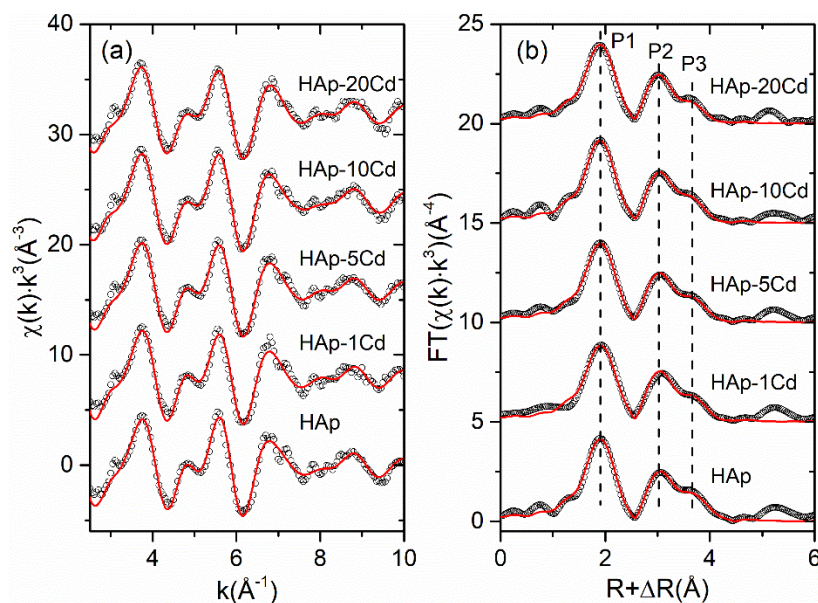
Figure 5. EXAFS spectra of k^3-weighted (a) and Fourier transform magnitudes (b) of the Ca K-edge in pure HAp and Cd-HAp samples. Dots are raw data and solid lines are structural fits.

268

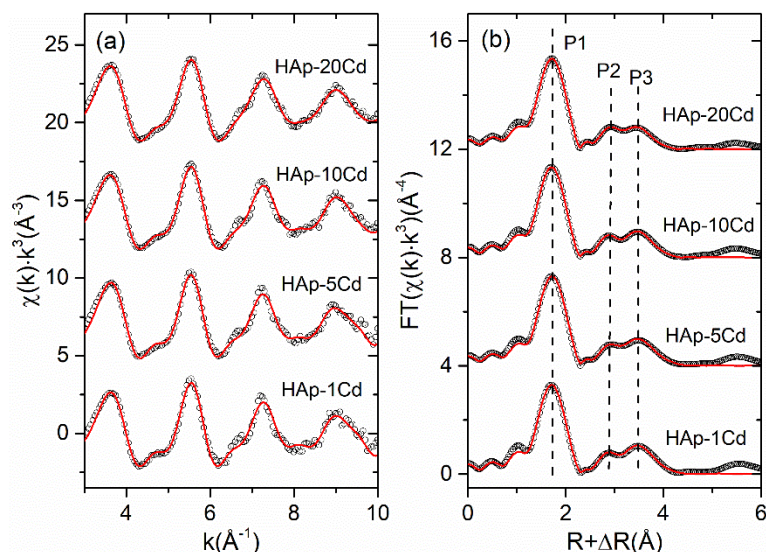**EXAFS spectra of the Cd K-edge in HAps**

There is no perceptible change due to Cd incorporation in XANES spectra of the Cd K-edge in Cd-HAp samples (Figure S8), implying that the local geometries are similar regardless of Cd content in HAps. The EXAFS spectra and structural fitting results for Cd in HAp samples are shown in Figure 6 and Table 2. The Fourier transforms of $k^3\chi(k)$ in R-space also exhibit three main peaks (Figure 6b), displaying that peak 1 (P1) is identical while a small but systematic increase in peak 2 (P2) and a decrease in peak 3 (P3). In comparison with the Ca K-edge spectra in pure Ca-HAp (Figure 5b), peak 2 in the Cd K-edge spectra is more intense than peak 3. In pure Ca-HAp, peak 2 results from the contribution of Ca···P (3rd shell) and Ca···Ca (4th shell) back-scattering, which are mainly derived from Ca1 as the center atom (Table S3) (Laurencin et al., 2011). In low Cd-HAp samples (HAp-1Cd, HAp-5Cd, and HAp-10Cd), peak 2 is relatively weak, indicating that Cd is located at the Ca2 site with only three P shells back-scattering

281   contributing to the low intensity of peak 2 (Lanfranco et al., 2003). However, in HAp-20Cd, the

282   increase in the peak 2 intensity indicates that the back-scattering from Cd at the Ca1 site also

283   contributes to this peak because Cd1 in Cd-HAp has the shortest Cd⋯Ca distance (Harries and

284   Hukins, 1986). This also confirms that in the Cd-HAp end member, Cd occupies all Ca1 and Ca2

285   sites, and EXAFS spectra of the Cd K-edge are similar to those of the Ca K-edge in both Ca- and

286   Cd-HAp end members, with a stronger peak 2 than peak 3 (Sery et al., 1996). Thus, because of

287   the weaker intensity of peak 2 than that of peak 3 in Cd-HAp, we deduce that Cd preferentially

288   occupies the Ca2 site in HAp at a low content, and the structural fittings of Cd-HAps are

289   conducted with Cd at the Ca2 site.

290   The fitting parameters listed in Table 2 show that peak 1 derived from two Cd⋯O shells

291   displays the shortest Cd-O distance of 2.28 Å, which is consistent with the reported shortest Ca-

292   O distance of Ca2 sites in pure Ca-HAp (Harries and Hukins, 1986). The fitting parameters of

293   the bond distance and Debye-Waller factor (σ^2) are quite similar in HAp-1Cd, HAp-5Cd, and

294   HAp-10Cd. The good fit assuming that Cd is located at the Ca2 site confirms that Cd

295   incorporates into the Ca2 site preferentially. However, the difference in the fifth shell of Cd⋯P

296   in HAp-20Cd has a shorter bond distance of 3.67 Å, which is much shorter than those of HAps

297   with low Cd contents. Since Cd at the Ca1 site has been reported to have a shorter Cd1⋯P

298   distance (Laurencin et al., 2011), the back-scattering of the surrounding P of Cd1 could make

299   fitted distance shorter. This could also result in an increase in the peak 2 intensity, suggesting

300   that Cd atoms also occupy Ca1 sites in HAps with high Cd contents.

301

Figure 6. EXAFS spectra of k^3-weighted (a) and Fourier transform magnitudes (b) of the Cd K-edge in Cd-HAp samples. Dots are raw data and solid lines are structural fits.

Table 2. Fitting parameters of the Cd K-edge EXAFS spectra in Cd-HAp samples with the model of Cd at the Ca2 site.

Atom/shell	HAp-1Cd			HAp-5Cd			HAp-10Cd			HAp-20Cd		
	N†	R (Å)	$\sigma^2(10^{-2}nm^2)$	N†	R (Å)	$\sigma^2(10^{-2}nm^2)$	N†	R (Å)	$\sigma^2(10^{-2}nm^2)$	N†	R (Å)	$\sigma^2(10^{-2}nm^2)$
O/1st	5	2.28	0.008	5	2.29	0.008	5	2.28	0.009	5	2.28	0.009
O/2nd	2	2.52	0.015	2	2.52	0.014	2	2.51	0.017	2	2.51	0.023
P/3rd	1	3.08	0.006	1	3.08	0.008	1	3.08	0.008	1	3.08	0.010
P/4th	2	3.38	0.025	2	3.37	0.028	2	3.42	0.032	2	3.37	0.028
P/5th	2	3.78	0.030	2	3.74	0.030	2	3.79	0.030	2	3.67	0.030
Ca/6th	6	3.97	0.010	6	3.98	0.011	6	3.97	0.013	6	3.96	0.015
Ca/7th	4	4.15	0.005	4	4.16	0.006	4	4.14	0.008	4	4.13	0.011

Note: † values fixed at averaged crystallographic values. Typical errors on the bond distances and Debye-Waller factors are ± 0.02 Å in R and 20% in σ^2, respectively.

309

DISCUSSION

Effect of Cd incorporation on the HAp crystal structure

The diffraction peaks shift and the lattice parameters (*a*, *c*, and *V*) linearly change with substituted Cd content, which mainly results from smaller radii of Cd^{2+} compared to Ca^{2+} (Bigi et al., 1986; Lanfranco et al., 2003). The decrease in intensity and the increase in width of the XRD peak (002) (Figure S2) indicate slightly decreased crystallinity due to Cd incorporation (Zhu et al., 2016). In contrast, several synthesized metal-substituted HAps with Mg^{2+} and Zn^{2+} suggest that the crystallinity of substituted HAps decreases obviously at 5% and 10% substitutions (Arul et al., 2018; Guerra-López et al., 2015), as both Mg^{2+} and Zn^{2+} have much smaller radius than Ca^{2+} (r_{Mg2+}=0.72 Å, r_{Zn2+}=0.74 Å, and r_{Ca2+}=1.00 Å). Interestingly, sorption experiments of Cd^{2+} and Zn^{2+} on HAp also indicate that Cd^{2+} could be more easily incorporated into the HAp structure than Zn^{2+} (Xu et al., 1994).

Changes in the local environment of phosphate in HAps due to Cd incorporation are reflected by modifications of peak position, FWHM, and intensity of Raman spectra. The redshift and broadening of $v_1(PO_4)$ are linearly correlated with Cd content. The v_1 (PO_4) mode was reported to correspond with the vibration in which P, O1, and O2 atoms were on the mirror plane and two O3 atoms at both sides of the plane (Antonakos et al., 2007). The incorporated Cd at the Ca2 site is bound with two next-nearest O3 atoms, producing a distortion of phosphate with slight decrease in the O3-P-O3 angle due to the smaller radius of Cd and the mass difference (Hata et al., 1978; Mercier et al., 2005). The distortion of phosphate bound with Cd results in redshifts and broadening of $v_1(PO_4)$, where both of them exhibit a linear relation with Cd content. The substitution of other cations in HAp was also reported to cause phosphate

332   distortions and induce a change in Raman spectra (Antonakos et al., 2017; Antonakos et al., 2007;

333   Stammeier et al., 2018; Terra et al., 2009). For other substituted cations, in comparison, a 3.2

334   mol% Zn substitution could cause a shift of 2 cm^{-1}, while the incorporated Cd with a content of

335   16.18 mol% only induces a 2 cm^{-1} shift, indicating that the effect of Cd^{2+} incorporation on the

336   symmetry distortion of phosphate tetrahedron is much weaker than Zn^{2+} due to similar radii of

337   Ca^{2+} and Cd^{2+} (Guerra-López et al., 2015; Lanfranco et al., 2003). Such effects of Cd

338   incorporation are also indicated by the decline in v_3(PO$_4$) peaks at 1025, 1045, and 1073 cm^{-1}

339   (Antonakos et al., 2017). However, the change induced by Cd incorporation is too slight to alter

340   the bond length of P-O even as the Cd content reaches 16.18 mol%. In that case, the slight

341   change only causes a small decrease in the shoulder peak (peak 2 in Figure S5) of the P K-edge

342   XANES spectra, and the P K-edge XANES analysis might not be sensitive enough to

343   differentiate the crystallinity of HAp with Cd incorporation (Chen and Arai, 2019). The small

344   difference between the ionic radii of Ca^{2+} and Cd^{2+} (only 0.04 Å) only changes the structure

345   slightly without disrupting the framework, which also contributes to the thermodynamic basis to

346   form completely continuous solid-solutions of Ca$_{10}$(PO$_4$)$_6$(OH)$_2$-Cd$_{10}$(PO$_4$)$_6$(OH)$_2$ (Pan and Fleet,

347   2002).

348

349   **Site preference of Cd incorporation into HAp**

350   Ca1 and Ca2 are crystallographically inequivalent sites in HAp, and both have the potential

351   for substitution of foreign ions. Although the preferred Ca site for different foreign ions is still

352   under debate, more studies have suggested that Ca2 is the preferred site based on Rietveld

353   analysis of XRD data and first principles calculations (Guerra-López et al., 2015; Lala et al.,

354   2015; Luo et al., 2009; Terra et al., 2010). In this study, the local environment of Ca and Cd in

355   HAp are investigated and the incorporation mechanism is revealed by combining Ca $L_{2,3}$-edge

356   TEY, Ca K-edge EXAFS, and Cd K-edge EXAFS analysis. The surrounding atomistic

357   environment of Ca with O is hardly altered by Cd incorporation (< 20 mol%), which has also

358   been confirmed in the Ca K-edge spectra of Mg-substituted HAp (Laurencin et al., 2011). The

359   similarity of the bond distance and coordination number of Ca in Cd-HAps confirms that Cd is

360   indeed at the Ca2 site, as reflected in the Ca $L_{2,3}$-edge TEY spectra. According to Ca $L_{2,3}$-edge

361   TEY spectra (Figure 4) and EXAFS spectra of the Cd K-edge (Figure 6b), we propose that Cd

362   atoms prefer to occupy the Ca2 site, and the reasonable fitting of r_{Cd-O}=2.28 Å is consistent with

363   the Cd2-O distance (2.28 Å) (Harries and Hukins, 1986). The higher electronegativity of Cd (1.7)

364   over Ca (1.0) results in a higher preference of Cd for Ca2 site to increase covalent interactions

365   with the hydroxyl oxygen bonding with Ca2 (Terra et al., 2010). Furthermore, theoretical

366   calculations have shown that Cd in Ca1 sites largely increases variation in the Cd-O distance

367   (Terra et al., 2010), which is opposite to the results of a similar Cd-O distance in EXAFS fitting

368   and a linear decrease in lattice parameters of Cd-HAps with increasing Cd content (Lanfranco et

369   al., 2003). Thus, the Ca2 site in HAp is preferential for Cd incorporation. However, the possible

370   limited content of incorporated Cd that only occupies Ca2 sites needs to be explored.

371   The spatial accommodation without disrupting the framework should be a key factor to

372   determine the site preference with different Cd contents (Pan and Fleet, 2002). From the

373   geometrical configuration of Ca2 atoms in the HAp structure, two adjacent triangles ($\triangle$, $\triangledown$)

374   with the nearest cations are shown to form one Ca2 hexagon (Figure S9 a, b). Occupancy at one

375   Ca2 site in the Ca2 hexagon reaches a Cd content of 10 mol%. Assuming homogenous

376   substitution of Cd without forming a Cd-Cd cluster in the HAp structure, substituted Cd should

377   first occupy Ca2 sites diagonally with the longest Cd-Cd bond distance in the Ca2 hexagon

378   (Figure S9c and d), in which the excess energy for the maximized Cd2-Cd2 distance is more

379   negative to favor this configuration (Terra et al., 2010). Thus, Cd atoms occupying two Ca2 sites

380   in one hexagon could reach 20 mol% of all Ca sites in HAp. However, our EXAFS analysis

381   indicates that Cd also occupies Ca1 sites in HAp-20Cd ($\geq$16.18 mol%), suggesting that only one

382   Ca2 site in the Ca2 hexagon is preferentially substituted by Cd. Then, with further increasing Cd

383   content above 10 mol%, Cd starts to occupy Ca1 sites after filling one Ca2 site in the Ca2

384   hexagon. Thus, 10 mol% is a limited Cd content for occupying Ca2 sites only, which is also

385   consistent with theoretical calculation results of excess energies that HAp with 10 mol% Cd has

386   the lowest excess energy with Cd occupying Ca2 sites compared to mixed Ca1/Ca2 sites and Ca1

387   sites (Terra et al., 2010). Hence, we propose a conceptual model for Cd incorporation in HAp at

388   different Cd contents (Figure 7). Cd ions first occupy hexagonal Ca2 positions since the Cd

389   content is lower than 10 mol% (Figure 7a). As the Cd content increases to 10-20 mol%, Cd ions

390   prefer to occupy the Ca1 site after one of the two Ca2 sites in each Ca2 hexagon is occupied

391   (Figures 7b and 7c). Furthermore, it is deduced that Cd could occupy all Ca2 and Ca1 sites

392   (Figure 7d) and eventually form the end member Cd-HAp ($Ca_0Cd_{10}(PO_4)_6(OH)_2$) (Hata et al.,

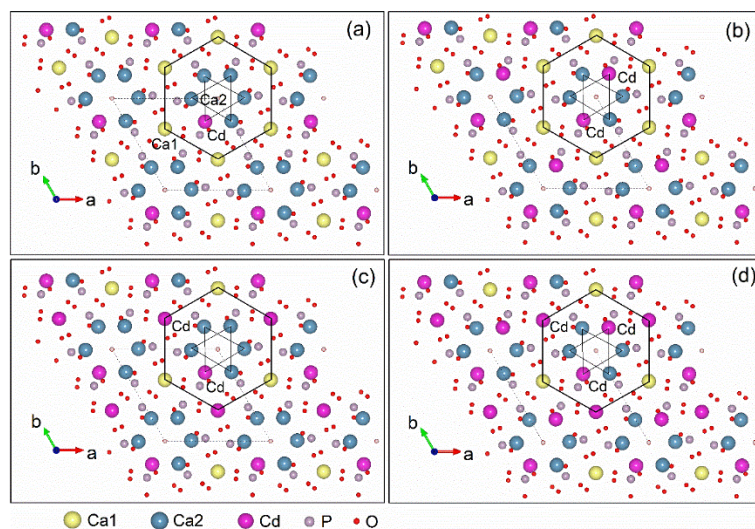393   1978; Lanfranco et al., 2003).

394

395   Figure 7. Representation of Cd incorporation into the HAp structure. (a) Cd in one Ca2 site (<10

396   mol%); (b) Cd in two Ca2 sites (10-20 mol%); (c) Cd in one Ca2 site and one Ca1 site (10-20

397   mol%); (d) Cd in two Ca2 sites and one Ca1 site (>20 mol%).

398

399   The effect of Cd preferentially at the Ca2 site may help us understand the change in lattice

400   parameters with Cd incorporation. The decrease of a and c parameters has a very good linear

401   relation with increasing Cd content at low Cd contents (<10 mol%), but shows a smaller

402   decreasing rate at a Cd content of 16 mol% (Figure S3), which may result from Cd at Ca2 with a

403   low Cd content and Cd at both Ca1/Ca2 sites with higher Cd contents. It has been reported that

404   pure Cd2 substitution results in smaller lattice parameters a and c than pure Cd1 substitution in

405   HAp (Tamm and Peld, 2006; Terra et al., 2010). This may explain our observed change in lattice

406   parameters a and c where the decrease rate is reduced at higher Cd contents (Figure S3). With

407   further increasing Cd content to form a complete Ca-Cd solid solution with mixed Cd2/Cd1

408   substitution, the change in lattice parameters becomes linear with Cd content in previous studies,

409   in which the increased interval of Cd content is approximately 10 mol% (Lanfranco et al., 2003;

410   Srinivasan et al., 2006; Terra et al., 2010).

411   The site preference of Cd in HAp also controls the dissolution process of Cd-HAp samples.

412   Reported dissolution experiments show that HAp samples with various Cd contents exhibit

413   different dissolution behaviors because of the preferred Ca sites for Cd (Zhu et al., 2016).

414   Average solubility products (K_{sp}) changes largely from $10^{-57.65}$ (pure HAp) to $10^{-59.18}$ (HAp with

415   8 mol% Cd), but changes slowly at higher Cd contents (Zhu et al., 2016). This study provides a

416   novel atomistic explanation that Cd only occupies the Ca2 site (<10 mol%) and alters kinetics for

417   surface ions release (Terra et al., 2010). The preferred Ca2 site for Cd substitution could enhance

418   Cd retention in the solid phase, as evidenced by sorption experiments, in which the sorption of

419   Cd^{2+} on HAp easily triggers coprecipitation of Cd-HAp (Srinivasan et al., 2006; Xu et al., 1994).

IMPLICATIONS

421   Cd is found to first occupy one Ca2 site at hexagonal Ca2 positions with Cd content lower

422   than 10 mol%, and then begin to occupy the Ca1 site with increasing Cd content. The Cd

423   incorporation only slightly changes the HAp long-range structure but increases structural

424   disorder. As reported previously, Cd could diffuse into HAp during Cd sorption by HAp and

425   form Cd-substituted HAp (Bailey et al., 2005; Xu et al., 1994). This study demonstrates that the

426   incorporated Cd affects the HAp structure less than other metals (e.g., Zn^{2+}), revealing that the

427   employment of HAp for Cd removal in contaminated water and soils should be effective. Natural

428   soils and water only contain trace amounts of Cd (commonly <500 mg/kg (McLaughlin and

429   Singh, 1999)), and the preferential occupancy of Ca2 via Cd under low Cd contents could

430   contribute to long-term retention of Cd.

431   Metal-substitution in various minerals plays key roles in geochemical and environmental

432   processes because substituted minerals commonly exhibit characteristics of both ions and modify

433   surface reactivity. Cu-substituted HAp has been reported to enhance arsenate sorption compared

434   to pure HAp (Liu et al., 2010). The increased surface area with Cd substitution suggests a

435   potential improvement in the sorption of toxic elements (e.g., Pb, Zn, As, etc.) by Cd-substituted

436   HAps. Additionally, the formation of solid-solutions has been widely employed to remove heavy

437   metals from groundwater and soils and fix these heavy metals in solid phases for long-term

438   remediation. Compared to surface adsorption, the Cd incorporation into the HAp structure

439   implies that the Cd release from Cd-substituted HAp must break the HAp framework, suggesting

440   that HAp could be a high-performance material for removing and storing Cd from contaminated

441   environments.

442

SUPPLEMENTAL MATERIAL

444   Supplemental Material includes structural model of HAp, lattice parameters, Raman results,

445   XANES spectra of P, Ca and Cd K-edge, fitting results of Ca $L_{2,3}$-edge TEY spectra,

446   representation model for Cd incorporation, and fitting parameters of EXAFS spectra.

447

ACKNOWLEDGMENTS

456   Ca and Cd. We are also grateful to Ms. Jiani Chen, Mr. Zhenmeng Sun, Dr. Xiaolin Wang, and

457   Ms. Ye Qiu for help with the analyses in TEM, BET, and Raman spectra.

458

459   **REFERENCES**

460   Ankoudinov, A.L. (1996) Relativistic Spin-dependent X-ray Absorption Theory (Ph.D. Thesis).

461   University of Washington.

462   Antonakos, A., Liarokapis, E., Kyriacou, A., and Leventouri, T. (2017) Raman and IR studies of

463   the effect of Fe substitution in hydroxyapatites and deuterated hydroxyapatite. American

464   Mineralogist, 102(1), 85-91.

465   Antonakos, A., Liarokapis, E., and Leventouri, T. (2007) Micro-Raman and FTIR studies of

466   synthetic and natural apatites. Biomaterials, 28(19), 3043-3054.

467   Arul, K.T., Ramesh, M., Chennakesavan, C., Karthikeyan, V., Manikandan, E., Umar, A., Maaza,

468   M., and Henini, M. (2018) Novel multifunctional of magnesium ions (Mg ++)

469   incorporated calcium phosphate nanostructures. Journal of Alloys and Compounds, 730,

470   31-35.

471   Bailey, E.H., Mosselmans, J.F.W., and Young, D. (2005) Time-dependent surface reactivity of

472   Cd sorbed on calcite, hydroxylapatite and humic acid. Mineralogical Magazine, 69(5),

473   563-575.

474   Beniash, E., Metzler, R.A., Lam, R.S.K., and Gilbert, P.U.P.A. (2009) Transient amorphous

475   calcium phosphate in forming enamel. Journal of Structural Biology, 166(2), 133-143.

476   Bigi, A., Gazzano, M., Ripamonti, A., Foresti, E., and Roveri, N. (1986) Thermal stability of

477   cadmium–calcium hydroxyapatite solid solutions. Journal of the Chemical Society,

478   Dalton Transactions(2), 241-244.

479   Chen, K.-Y. and Arai, Y. (2019) X-ray Diffraction and X-ray Absorption Near-Edge Structure

480   Spectroscopic Investigation of Hydroxyapatite Formation under Slightly Acidic and

481   Neutral pH Conditions. ACS Earth and Space Chemistry 3(10): 2266-2275.

482   Cosmidis, J., Benzerara, K., Nassif, N., Tyliszczak, T., and Bourdelle, F. (2015) Characterization

483   of Ca-phosphate biological materials by scanning transmission X-ray microscopy (STXM)

484   at the Ca $L_{2,3}$-, P $L_{2,3}$- and C K-edges. Acta Biomaterialia, 12, 260-269.

485   da Rocha, N.C.C., de Campos, R.C., Rossi, A.M., Moreira, E.L., Barbosa, A.d.F., and Moure,

486   G.T. (2002) Cadmium uptake by hydroxyapatite synthesized in different conditions and

487   submitted to thermal treatment. Environmental science & technology, 36(7), 1630-1635.

488   Goldhammer, T., Brüchert, V., Ferdelman, T.G., and Zabel, M. (2010) Microbial sequestration

489   of phosphorus in anoxic upwelling sediments. Nature Geoscience, 3(8), 557-561.

490   Guerra-López, J.R., Echeverría, G.A., Güida, J.A., Viña, R., and Punte, G. (2015) Synthetic

491   hydroxyapatites doped with Zn(II) studied by X-ray diffraction, infrared, Raman and

492   thermal analysis. Journal of Physics and Chemistry of Solids, 81, 57-65.

493   Harries, J.E., and Hukins, D.W.L. (1986) Analysis of the EXAFS spectrum of hydroxyapatite.

494   Journal of Physics C: Solid State Physics, 19(34), 6859-6872.

495   Harries, J.E., Hukins, D.W.L., and Hasnain, S.S. (1988) Calcium environment in bone mineral

496   determined by EXAFS spectroscopy. Calcified tissue international, 43(4), 250-253.

497   Hata, M., Okada, K., Iwai, S., Akao, M., and Aoki, H. (1978) Cadmium hydroxyapatite. Acta

498   Crystallographica Section B: Structural Crystallography and Crystal Chemistry, 34(10),

499   3062-3064.

500   Hughes, J.M., Cameron, M., and Crowley, K.D. (1989) Structural variations in natural F, OH,

501   and Cl apatites. American Mineralogist, 74(7-8), 870-876.

502   Hughes, J.M., and Rakovan, J.F. (2015) Structurally robust, chemically diverse: apatite and

503   apatite supergroup minerals. Elements, 11(3), 165-170.

504   Kay, M.I., Young, R.A., and Posner, A.S. (1964) Crystal structure of hydroxyapatite. Nature,

505   204(4963), 1050-1052.

506   Kim, Y., Konecke, B., Fiege, A., Simon, A., and Becker, U. (2017) An ab-initio study of the

507   energetics and geometry of sulfide, sulfite, and sulfate incorporation into apatite: The

508   thermodynamic basis for using this system as an oxybarometer. American Mineralogist,

509   102(8), 1646-1656.

510   Kobayashi, J. (1978) Pollution by cadmium and the itai-itai disease in Japan. In Toxicity of

511   Heavy Metals in the Environment, pp. 199-260. Marcel Dekker, Inc., New York.

512   Lala, S., Ghosh, M., Das, P.K., Kar, T., and Pradhan, S.K. (2015) Mechanical preparation of

513   nanocrystalline biocompatible single-phase Mn-doped A-type carbonated hydroxyapatite

514   (A-cHAp): effect of Mn doping on microstructure. Dalton Transactions , 44(46), 20087-

515   97.

516   Lanfranco, A.M., Schofield, P.F., Murphy, P.J., Hodson, M.E., Mosselmans, J.F.W., and

517   Valsami-Jones, E. (2003) Characterization and identification of mixed-metal phosphates

518   in soils: the application of Raman spectroscopy. Mineralogical Magazine, 67(6), 1299-

519   1316.

520   Larson, A.C., and Von Dreele, R.B. (2000) General Structure Analysis System (GSAS). Los

521   Alamos National Laboratory Report LAUR, 86-748.

522   Laurencin, D., Almora-Barrios, N., de Leeuw, N.H., Gervais, C., Bonhomme, C., Mauri, F.,

523   Chrzanowski, W., Knowles, J.C., Newport, R.J., and Wong, A. (2011) Magnesium

524   incorporation into hydroxyapatite. Biomaterials, 32(7), 1826-1837.

525   Lee, H.H., Owens, V.N., Park, S., Kim, J., and Hong, C.O. (2018) Adsorption and precipitation

526   of cadmium affected by chemical form and addition rate of phosphate in soils having

527   different levels of cadmium. Chemosphere, 206, 369-375.

528   Liu, G., Talley, J.W., Na, C., Larson, S.L., and Wolfe, L.G. (2010) Copper Doping Improves

529   Hydroxyapatite Sorption for Arsenate in Simulated Groundwaters. Environmental

530   Science & Technology, 44(4), 1366-1372.

531   Liu, J., Yang, J., Cade-Menun, B.J., Hu, Y., Li, J., Peng, C., and Ma, Y. (2017) Molecular

532   speciation and transformation of soil legacy phosphorus with and without long-term

533   phosphorus fertilization: Insights from bulk and microprobe spectroscopy. Scientific

534   Reports, 7(1), 15354.

535   Lowry, N., Han, Y., Meenan, B.J., and Boyd, A.R. (2017) Strontium and zinc co-substituted

536   nanophase hydroxyapatite. Ceramics International, 43(15), 12070-12078.

537   Luo, Y., Hughes, J.M., Rakovan, J., and Pan, Y. (2009) Site preference of U and Th in Cl, F, and

538   Sr apatites. American Mineralogist, 94(2-3), 345-351.

539   Matsunaga, K., Murata, H., Mizoguchi, T., and Nakahira, A. (2010) Mechanism of incorporation

540   of zinc into hydroxyapatite. Acta Biomater, 6(6), 2289-93.

541   McLaughlin, M.J., and Singh, B.R. (1999) Cadmium in soils and plants. Cadmium in soils and

542   plants, pp. 1-9. Springer.

543   Mercier, P. H., Le Page, Y., Whitfield, P. S., Mitchell, L. D., Davidson, I. J., & White, T. J.

544   (2005). Geometrical parameterization of the crystal chemistry of P63/m apatites:

545   comparison with experimental data and ab initio results. Acta Crystallographica Section

546   B: Structural Science, 61(6), 635-655.

547   Naftel, S., Sham, T., Yiu, Y., and Yates, B. (2001) Calcium L-edge XANES study of some

548   calcium compounds. Journal of synchrotron radiation, 8(2), 255-257.

549   Neuville, D.R., Cormier, L., Flank, A.M., Briois, V., and Massiot, D. (2004) Al speciation and

550   Ca environment in calcium aluminosilicate glasses and crystals by Al and Ca K-edge X-

551   ray absorption spectroscopy. Chemical Geology, 213(1), 153-163.

552   Pan, Y., and Fleet, M.E. (2002) Compositions of the apatite-group minerals: substitution

553   mechanisms and controlling factors. Reviews in Mineralogy and Geochemistry, 48(1),

554   13-49.

555   Peld, M., Tõnsuaadu, K., and Bender, V. (2004) Sorption and Desorption of Cd^{2+} and Zn^{2+} Ions

556   in Apatite-Aqueous Systems. Environmental Science & Technology, 38(21), 5626-5631.

557   Petit, S., Gode, T., Thomas, C., Dzwigaj, S., Millot, Y., Brouri, D., Krafft, J.M., Rousse, G.,

558   Laberty-Robert, C., and Costentin, G. (2017) Incorporation of vanadium into the

559   framework of hydroxyapatites: importance of the vanadium content and pH conditions

560   during the precipitation step. Phys Chem Chem Phys, 19(14), 9630-9640.

561   Politi, Y., Metzler, R.A., Abrecht, M., Gilbert, B., Wilt, F.H., Sagi, I., Addadi, L., Weiner, S.,

562   and Gilbert, P. (2008) Transformation mechanism of amorphous calcium carbonate into

563   calcite in the sea urchin larval spicule. Proceedings of the National Academy of Sciences,

564   105(45), 17362-17366.

565   Prietzel, J., Dümig, A., Wu, Y., Zhou, J., and Klysubun, W. (2013) Synchrotron-based P K-edge

566   XANES spectroscopy reveals rapid changes of phosphorus speciation in the topsoil of

567   two glacier foreland chronosequences. Geochimica et Cosmochimica Acta, 108, 154-171.

568   Ravel, B., and Newville, M. (2005) ATHENA, ARTEMIS, HEPHAESTUS: data analysis for X-

569   ray absorption spectroscopy using IFEFFIT. Journal of Synchrotron Radiation, 12(4),

570   537-541.

571   Sery, A., Manceau, A., and Greaves, N. (1996) Chemical state of Cd in apatite phosphate ores as

572   determined by EXAFS spectroscopy. American Mineralogist, 81, 864-873.

573   Shannon, R.D. (1976) Revised effective ionic radii and systematic studies of interatomic

574   distances in halides and chalcogenides. Acta Crystallographica Section A: Crystal

575   Physics, Diffraction, Theoretical and General Crystallography, A32(5), 751-767.

576   Skwarek, E., and Janusz, W. (2016) Adsorption of Cd (II) ions at the hydroxyapatite/electrolyte

577   solution interface. Separation Science and Technology, 51(1), 11-21.

578   Srinivasan, M., Ferraris, C., and White, T. (2006) Cadmium and Lead Ion Capture with Three

579   Dimensionally Ordered Macroporous Hydroxyapatite. Environmental Science &

580   Technology, 40(22), 7054-7059.

581   Stammeier, J.A., Purgstaller, B., Hippler, D., Mavromatis, V., and Dietzel, M. (2018) In-situ

582   Raman spectroscopy of amorphous calcium phosphate to crystalline hydroxyapatite

583   transformation. MethodsX, 5, 1241-1250.

584   Tamm, T., and Peld, M. (2006) Computational study of cation substitutions in apatites. Journal

585   of Solid State Chemistry, 179(5), 1581-1587.

586   Terra, J., Dourado, E.R., Eon, J.G., Ellis, D.E., Gonzalez, G., and Rossi, A.M. (2009) The

587   structure of strontium-doped hydroxyapatite: an experimental and theoretical study.

588   Physical Chemistry Chemical Physics, 11(3), 568-577.

589   Terra, J., Gonzalez, G.B., Rossi, A.M., Eon, J.G., and Ellis, D.E. (2010) Theoretical and

590   experimental studies of substitution of cadmium into hydroxyapatite. Physical Chemistry

591   Chemical Physics, 12(47), 15490-15500.

592   Toby, B.H. (2001) EXPGUI, a graphical user interface for GSAS. Journal of applied

593   crystallography, 34(2), 210-213.

594   Valsami-Jones, E., Ragnarsdottir, K.V., Putnis, A., Bosbach, D., Kemp, A.J., and Cressey, G.

595   (1998) The dissolution of apatite in the presence of aqueous metal cations at pH 2–7.

596   Chemical Geology, 151(1-4), 215-233.

597   Wang, M., Wu, S., Guo, J., Zhang, X., Yang, Y., Chen, F., and Zhu, R. (2019) Immobilization of

598   cadmium by hydroxyapatite converted from microbial precipitated calcite. Journal of

599   hazardous materials, 366, 684-693.

600   Wilson, R.M., Elliott, J.C., and Dowker, S.E.P. (1999) Rietveld refinement of the

601   crystallographic structure of human dental enamel apatites. American mineralogist, 84(9),

602   1406-1414.

603   Xu, Y., Schwartz, F.W., and Traina, S.J. (1994) Sorption of Zn2+ and Cd2+ on Hydroxyapatite

604   Surfaces. Environmental Science & Technology, 28(8), 1472-1480.

605   Yang, T., Wen, W., and Yin, G. (2015) Introduction of the X-ray diffraction beamline of SSRF.

606   Nuclear Science and Techniques, 26(2), 020101.

607   Zhang, J.Z., Guo, L., and Fischer, C.J. (2010) Abundance and Chemical Speciation of

608   Phosphorus in Sediments of the Mackenzie River Delta, the Chukchi Sea and the Bering

609   Sea: Importance of Detrital Apatite. Aquatic Geochemistry, 16(3), 353-371.

610   Zhang, L., Xu, Z., Zhang, X., Yu, H., Zou, Y., Guo, Z., Zhen, X., Cao, J., Meng, X., Li, J., Chen,

611   Z., Wang, Y., and Tai, R. (2015) Latest advances in soft X-ray spectromicroscopy at

612   SSRF. Nuclear Science and Techniques, 26, 040101.

613   Zhu, Y., Zhu, Z., Zhao, X., Liang, Y., Dai, L., and Huang, Y. (2016) Characterization,

614   dissolution and solubility of cadmium–calcium hydroxyapatite solid solutions at 25 C.

615   Chemical Geology, 423, 34-48.

616   Zilm, M.E., Chen, L., Sharma, V., McDannald, A., Jain, M., Ramprasad, R., and Wei, M. (2016)

617   Hydroxyapatite substituted by transition metals: experiment and theory. Phys. Chem.

618   Chem. Phys., 18(24), 16457-16465.

619   Zougrou, I.M., Katsikini, M., Brzhezinskaya, M., Pinakidou, F., Papadopoulou, L., Tsoukala, E.,

620   and Paloura, E.C. (2016) Ca $L_{2,3}$-edge XANES and Sr K-edge EXAFS study of

621   hydroxyapatite and fossil bone apatite. The Science of Nature, 103(7), 60.

622